

Prospects for NMR Spectral Prediction on Fault-Tolerant Quantum Computers

J. E. Elenewski,^{1,*} C. M. Camara,² and A. Kalev^{3,4,†}

¹*MIT Lincoln Laboratory, Lexington, Massachusetts 02421, USA*

²*Department of Pediatric Oncology and the Linde Program in Cancer Chemical Biology, Dana-Farber Cancer Institute, Boston, MA, USA*

³*Information Sciences Institute, University of Southern California, Arlington, VA 22203, USA*

⁴*Department of Physics and Astronomy, and Center for Quantum Information Science & Technology, University of Southern California, Los Angeles, California 90089, USA*

Nuclear magnetic resonance spectroscopy is a prominent analytical tool, with applications throughout chemistry, medicine and solid-state physics. While conventional NMR spectrometers require large magnetic fields to interrogate a sample, recent advances in atomic magnetometry have enabled this spectroscopy far below geomagnetic field strengths. This zero-to-ultralow (ZULF) field regime can be advantageous since it mitigates relaxation and reveals spin couplings that are otherwise obscured, all while using compact and lower-overhead instrumentation. The resulting spectra are nonetheless difficult to interpret without computation, which can be taxing due to the presence of vector couplings and long-range spin networks. Following recent proposals, we demonstrate how fault-tolerant quantum computation could be used to simulate these spectra. Our analysis spans from input selection to the construction of explicit circuits based on qubitized quantum dynamics. By maintaining parity with experimental requirements, we demonstrate how NMR spectral prediction might be an early application for fault-tolerant quantum computers.

Nuclear magnetic resonance (NMR) spectroscopy has become entrenched as an analytical tool in chemistry, physics, and materials science. Notably, this technique can resolve atomic-scale structures and dynamics across a hierarchy of timescales (10^{-11} – 10^0 s), giving a fingerprint to identify samples and a means to probe their underlying physics [1]. The ability to accommodate diverse analytes has made these spectra a characterization requirement for many classes of small molecules and materials. Advances in high-field magnets and signal processing have also extended this capability to polymers, supramolecular assemblies and biological macromolecules [2–4]. This has delivered some of the most detailed protein structures to date and provided decisive insights into molecular biophysics [2, 5–11]. Spatially-resolved NMR [12–14] and magnetic resonance imaging (MRI) have likewise become standard diagnostic tools in medicine [15–17].

Unfortunately, most NMR spectrometers are sizable, expensive, and require nontrivial infrastructure. The most accessible are lower-field spectrometers, which are comparatively small and inexpensive (< 100K USD). However, these are limited to low-resolution or quality control applications. High-field instruments are often needed to resolve spin cou-

plings and complicated spectra, and have a much higher cost of ownership (1M to 10M USD). The resulting data can be cumbersome to interpret, requiring complimentary experiments and dedicated expertise for complicated systems. These factors can limit application domains and accessible analytes.

The development of NMR has followed a quest for higher spectral resolution. This has led to spectrometers with large static magnetic fields, B_0 , which give a broad frequency dispersion $\Delta\omega \sim B_0$ among resonances and increase the fraction $P \sim B_0/k_B T$ of polarized spins [1, 5]. More recently, advances in atomic magnetometry have raised the possibility of spectroscopy in low- (30–50 μ T) or zero-to-ultralow field regimes (ZULF; below 100 nT) [18–20]. Here, hyperpolarization can access super-thermal spin populations ($P \sim 10^{-1}$) that exceed those from high-field magnets ($P \sim 10^{-3}$) [21]. These spectrometers are also comparatively inexpensive, portable, and capable of cryogen-free operation. While ZULF can mitigate relaxation and reveal high-resolution couplings [22] that capture different physics [23, 24], this regime differs markedly from high-field NMR [25]. Notably, these spectra are hard to interpret without computation, which is costly since we must deal with long-range Heisenberg-like Hamiltonians.

The primary output of an NMR experiment is the time-domain free-induction decay (FID) signal $S(t) = \text{FID}(t)$, which quantifies current induced in a

* justin.elenewski@ll.mit.edu

† amirk@isi.edu

series of RF pickup coils. However, the interpretable spectrum is actually its sparse, frequency-domain counterpart $\mathcal{S}(\omega) = \int_0^{t_{\max}} \mathcal{S}(t) e^{i\omega t} dt$. In principle this can be obtained by simulating a spin-spin correlation function,

$$\langle S_{\text{tot}}(t) S_{\text{tot}}(0) \rangle = \text{tr} [e^{iHt} S_{\text{tot}} e^{-iHt} S_{\text{tot}} \rho], \quad (1)$$

where the k -spin system is described by a Heisenberg Hamiltonian H and density matrix ρ . Here, the operator $S_{\text{tot}} = \sum_k S_k$ captures a total spin. A typical NMR experiment uses phase-sensitive quadrature to detect $S^+ = S^x + iS^y$, but this is due to the apparatus and the control pulse sequence. Simply calculating a spectrum only requires us to observe S^z and thus we can use $S_{\text{tot}} = S_{\text{tot}}^z = \sum_k S_k^z$ for the total spin [26]. Our predicted result $\tilde{\mathcal{S}}(\omega)$ follows immediately,

$$\tilde{\mathcal{S}}(\omega) = \int_0^{t_{\max}} \langle S_{\text{tot}}^z(t) S_{\text{tot}}^z(0) \rangle e^{i\omega t - \gamma_2 t} dt. \quad (2)$$

The factor containing $\gamma_2 = T_2^{-1}$ captures relaxation processes that lead to decoherence and dephasing. This can also be accommodated by introducing a relaxation superoperator, though the present case is simpler for analysis.

Based on the above, simulating NMR spectra is inherently an exerciser in quantum dynamics. However, since the underlying Hamiltonian is a long-range Heisenberg model, the calculations can become classically hard for tens of coupled spins. This is true for ZULF spectra as well as other problems such as solid-state NMR and high-field NMR with strongly coupled spin systems [27]. Owing to this, the calculation of ZULF and nitrogen-vacancy NMR spectra have been touted as possible applications for NISQ-scale quantum computers [28–30].

We extend these efforts to fault-tolerant quantum computation and explore the overhead in simulating ZULF spectra for a broad range of high-value molecular targets. Our approach utilizes state-of-the-art algorithms for quantum dynamics — based on quantum signal processing — and leverages optimized encodings to mitigate resource requirements. Moreover, we address efficient protocols for reconstructing spectra (using compressed sensing techniques) and the prospects of pulse sequence design. Our estimates indicate that meaningful spectra might be computed with resource overhead comparable or below other problems, such as factoring 2048-bit integers using Shor’s algorithm [31] or simulating classically hard instances of the Fermi-Hubbard model. This suggests that NMR spec-

tral prediction is a robust, near-term application for fault-tolerant hardware.

I. BACKGROUND AND CONTEXT

A. NMR Hamiltonian

A foundational assumption for NMR is that nuclear spin evolution can be separated from the corresponding electron dynamics [1]. This is reasonable since electrons outpace the nuclei by several orders of magnitude. However, the electronic subsystem still mediates nuclear spin couplings through time-averaged parameters. Based on this, our discussion will assume the usual Hamiltonian for a system of N nuclear spins:

$$H = H_{\text{Zeeman}} + H_{\text{RF}} + H_J + H_D. \quad (3)$$

The first term, H_{Zeeman} , captures coupling to a static, external magnetic field $\mathbf{B}_0 = (0, 0, B_{z0})$ through a Zeeman contribution,

$$\begin{aligned} H_{\text{Zeeman}} &= -\hbar \sum_k \gamma_k (1 - \delta_k) \mathbf{I}_k \cdot \mathbf{B}_0 \\ &= \hbar \sum_k \omega_{0k} I_k^z. \end{aligned} \quad (4)$$

Note that we follow a convention where \mathbf{B}_0 lies along the z -axis, which will also be the quantization axis for our spin system. We also define $\mathbf{I}_k = \mathbf{S}_k / \hbar = (S_k^x, S_k^y, S_k^z) / \hbar$ to be a vector of spin angular momentum operators $S^\alpha = \hbar \sigma^\alpha / 2$ acting on the k -th spin, where σ^α is the corresponding Pauli matrix. Other factors include the nuclear gyromagnetic ratio for the k -th atom, γ_k , and the diamagnetic shielding tensor, δ_k . The latter is highly sensitive to the electronic environment surrounding each nucleus, arising from effects such as paramagnetic spin-orbit coupling and higher-order diamagnetic interactions. The second line in Eq. 4 applies to the liquid phase, where rotational averaging allows us to introduce $\omega_{0k} = -\gamma_k (1 - \delta_k^{zz}) B_{0z}$ as the isotropic chemical shift of the k -th nucleus. Chemical shifts depend on the specific nucleus and its location in a molecule, and generally range between 10^2 – 10^5 Hz (Fig. 1). Resonances near these frequencies are the most apparent features in high-field NMR spectra.

A similar expression describes RF control, which appears through the term H_{RF} in Eq. 3:

$$H_{\text{RF}} = -\hbar \sum_k \gamma_k \mathbf{I}_k \cdot \mathbf{B}_{\text{RF}}(t). \quad (5)$$

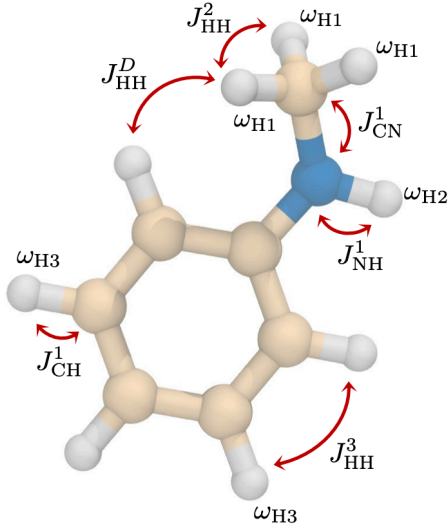


FIG. 1. **Components of a nuclear spin Hamiltonian.** Representative chemical shifts and couplings, as illustrated using the organic molecule *N*-methylaniline. Chemically equivalent protons share the same chemical shift, which are labeled for ω_{H1} , ω_{H2} , and ω_{H3} . Electronically-mediated J -couplings are shown for select homonuclear (J_{HH}^n) and heteronuclear cases (J_{CH}^n , J_{NH}^n). These differ in the number of intermediate bonds n between coupled spins. A dipolar coupling J_{HH}^D is also shown. Dipolar couplings can exist between atoms with a spatial separation ≤ 5 Å, even if they are J -coupled.

Here, $\mathbf{B}_{RF}(t)$ is the magnetic component of a classical RF pulse (generally with linear polarization). This term is required when simulating the response to a given control sequence, though it is not necessary when predicting spectral resonances. We will set $H_{RF} = 0$ when doing the latter.

Nuclear spins couple through the H_J and H_D terms, which differ in terms of prominence and prevalence for detected spectra. The weakest yet most detectable is an effective hyperfine coupling,

$$H_J = \hbar \sum_{k < l} \mathbf{I}_k \cdot \mathbf{J}_{kl} \cdot \mathbf{I}_l, \quad (6)$$

that is mediated by the electronic environment surrounding a pair of chemically bonded atoms. Couplings between spins k and l are encoded by the tensor \mathbf{J}_{kl} , where we abuse notation and use a dot to denote contraction (following standard NMR literature). This acts as a perturbation to the Zeeman term in high-field spectra, splitting resonances that are detected at chemical shift frequencies. Thus, the measured couplings are a sensitive probe of

the spin neighborhood and hence the local molecular geometry (Fig. 1). We can decompose this further into isotropic and anisotropic components $H_J = H_{J,iso.} + H_{J,aniso.}$ as:

$$H_{J,iso.} = \hbar \sum_{k < l} J_{kl} \mathbf{I}_k \cdot \mathbf{I}_l \quad (7)$$

$$H_{J,aniso.} = \hbar \sum_{k < l} \mathbf{I}_k \cdot \mathbf{J}_{kl}^{aniso.} \cdot \mathbf{I}_l. \quad (8)$$

The anisotropic contribution will be negligible for our purposes, and thus Eq. 7 is sufficient to the coupling between bonded spins. The scalar coupling J_{kl} is on the order of 1 Hz to 10^3 Hz.

The last term H_D contains a magnetic dipolar coupling between spatially-proximate spins,

$$H_D = \sum_{k < l} b_{kl} \left[\mathbf{I}_k \cdot \mathbf{I}_l - 3 \frac{1}{|\mathbf{r}_{kl}|^2} (\mathbf{I}_k \cdot \mathbf{r}_{kl})(\mathbf{I}_l \cdot \mathbf{r}_{kl}) \right], \quad (9)$$

which affects bonded and nonbonded pairs of atoms. Here b_{kl} is a dipolar coupling strength and \mathbf{r}_{kl} is a vector between the k -th and l -th nuclei. Note that we have absorbed the spatial dependence into the dipolar coupling $b_{kl} = \mu_0 \gamma_k \gamma_l \hbar / 4\pi |\mathbf{r}_{kl}|^3$. These contributions are can be detected for atoms separated by less than 5 Å.

B. (Ultra)Low- vs. High-Field NMR Spectroscopy

High-field NMR spectra are acquired by using RF pulses to (i) generate Rabi oscillations when tuned to the shielded Larmor frequency ω_{0k} of each nucleus and (ii) to induce and invert a transverse magnetization profile that is detected by the spectrometer. The resulting spectra exhibit resonances near the shielded Larmor frequencies (chemical shifts) for each nucleus. Spin-spin couplings can split these resonances into detuned satellite features or cross-resonances in multidimensional spectra. This coupling data is rich, as it reflects spatial connectivity and dynamic processes within the sample.

These conventional spectra are dominated by chemical shifts, in that the perturbations from coupling are several orders of magnitude smaller than the shifts. Thus, the resonances at each shift can be used to earmark a set of chemically distinct atoms, while their connectivity can be inferred from the couplings. In contrast, ZULF experiments invert this paradigm by giving spectra that are dominated by spin-couplings. A particularly striking aspect is that

the chemical shift dispersion $\Delta\omega$ becomes smaller than the spectral linewidth (roughly 20 Hz for ^1H), and thus spectra are centered on a common feature with peaks that are determined by intricate spin interactions. This complexity is more than superficial, as conventional NMR and ZULF each probe fundamentally different physical regimes [25]. Owing to this, experiments in this latter are sometimes referred to as J -coupling spectroscopy.

The virtue of ZULF extends beyond its comparatively inexpensive and cryogen-free instrumentation. Notably, these experiments avoid relaxation effects that arise from field inhomogeneities, chemical shift anisotropy and dipolar coupling [22]. Certain spectral features also become more apparent, including select heteronuclear dipolar couplings that are masked in high-field experiments [23, 24]. Spin coupling patterns can also become easier to identify. An additional virtue exists for ZULF-based imaging, where low field frequencies can circumvent skin effects when imaging metal samples or through metals.

C. Classical Limitations

Simulating NMR spectra is an exercise in quantum dynamics, which can be formally hard irrespective of the field regime. In the most naïve sense, the requisite evolution amounts to exponentiating a $2^N \times 2^N$ matrix. Of course, realistic systems have structures that can be leveraged to reduce complexity, such as the clustered topology of real spin interaction networks. High-field NMR spectrometers (9 T to 20 T) also operate a regime where it is often safe to ignore contributions that do not commute with the Zeeman term, reducing vector spin couplings to scalar $S_i^z S_k^z$ terms. This gives a considerable reduction in computational overhead. By leveraging the effects of decoherence / dephasing and restricted state-space approximations, state-of-the-art codes like Spinach can simulate certain NMR experiments for several thousand coupled spins [32, 33]. A further simplification is to consider the evolution of isolated subsystems by specific control pulse sequences. This can decouple other components of the spin system, making simulation inexpensive and interpretation intuitive [1, 5]. However, even high-field, liquid-phase spectra can become difficult for highly correlated spin systems [27].

Low-field and ZULF experiments do not benefit from many of these assumptions [25]. From the outset, spin couplings must remain a vector interaction $\mathbf{I}_j \cdot \mathbf{I}_k$ which makes the problem equivalent

to a Heisenberg model instead of an Ising model. Moreover, ZULF spectroscopy’s considerably longer relaxation timescales will minimize the classical simulation advantages that noise would lend by reducing fidelity targets [23, 34]. Approximations that disregard certain spin couplings are also unacceptable, as these quantities are specifically targeted by ZULF spectroscopy [22]. The increased prominence of dipolar couplings becomes an additional complication [24] for classical simulation. Notably, the conjunction of slow relaxation with long-range interactions can confound tensor network simulators [35, 36].

D. Utility

1. Computational Utility

ZULF experiments can compliment their high-field counterparts in some applications and might one day replace them in others [19]. However, this technique is partially bottlenecked by difficulties in predicting and interpreting spectra. Immediate advantages appear in the spectra themselves, where spin couplings can be extracted with extremely high precision [22, 37]. This consideration also holds for heteronuclear dipolar couplings that are unmasked in ZULF experiments [24]. Both of, these data can be extremely useful when determining high-resolution molecular structures. The unique nature of ZULF also has the potential to allow the direct determination of molecular chirality, which otherwise requires a cumbersome auxiliary compound [38]. Even the most prosaic application of a low-cost, benchtop J -coupling spectrometer could reduce turnaround in a chemical research setting. Nonetheless, these tasks require simulation to assign resonance peaks and fit candidate structures to spectra [37].

Eliminating costly superconducting magnets and cryogenic systems can lead to smaller, lower-cost NMR spectrometers. This is a substantial advantage of ZULF technologies. These instruments might enjoy broad use in field-use settings (e.g., environmental monitoring, forensic, and CBRN / defense applications), particularly when the goal is to screen an analyte against known molecular fingerprints. This market is currently addressed by portable optical (infrared, Raman) and mass spectrometers, though NMR provides a complimentary and discerning technique. Small NMR spectrometers could be useful when quantifying hazardous materials like explosives

or chemical warfare agents, particularly when encountering a new compound. In this case, the ability to sequester the instrument in a controlled environment is especially valuable. While all molecular fingerprinting applications require experimental reference spectra or simulations, the latter is a standout for particularly hazardous materials.

There are additional advantages for ZULF in laboratory, clinical, and production settings. For instance, these spectrometers can be used alongside systems for real-time reaction monitoring [39, 40], which is difficult with a bulky high-field spectrometer. ZULF’s insensitivity to sample inhomogeneity (e.g., magnetic susceptibility variations) [24, 41] or conductive environments [42] also permits integration into analytical systems like stopped flow mixers, where metal components or strong electrolytes could be present. This is likewise advantageous for medical diagnostics or manufacturing processes where NMR spectroscopy is has been difficult to apply. The same considerations can extend to whole-device metrologies – which has especially strong relevance for emerging battery materials – and spatially-resolved magnetic resonance imaging.

The ZULF setting can also host techniques that are difficult to engineer with conventional NMR. Notably, the possibility for exploiting robust quantum control might deliver new opportunities for nanoscale measurement and imaging [43, 44]. Similar considerations hold for more exotic magnetic resonance processes, such as β - or γ -NMR, which have proven valuable for materials diagnostics.

2. Domain Specific Utility: Drug Discovery Workflow

We consider two workflows when making our resource estimates. The most straightforward is a small-molecule drug-discovery workflow, which captures the domain specific impact of ZULF spectrometers. The fruits of this effort would be particularly valuable, as roughly 90% of marketed drugs are small molecules. To start, we can assume that a given drug discovery pipeline might handle up to 5000 distinct compounds that would benefit from ZULF NMR in a single year (or require multiple ZULF experiments with smaller, more complex molecule sets). Assuming that computation is utilized for each of these compounds, a useful turnaround time for each spectral prediction would be within 48 hours. Complex molecules – e.g., natural products which require elucidation – could enjoy a longer timeframe on the order of one to two weeks. A major pharmaceutical may have 10 robust small-molecule pipelines,

and thus 5×10^4 compounds may be analyzed annually. Conversely, a startup may have a single notable pipeline.

The United States has capitalized 56% percent of the top 25 pharmaceutical companies, so we will assume that there are 13 major domestic drug manufacturers (albeit with varied degrees of internal research and development) [45–47]. There are also more than 5000 pharmaceutical, biotechnology, and pharmaceutical-supporting enterprises in the US, which are equal or smaller in research volume. We assume that half of these address small-molecule research in some manner. A good approximation is to treat this contribution as 2500 startup-scale projects with the equivalent of a single robust small-molecule pipeline (even if this is actually adjacent research, e.g., diagnostics, research tool, or adjuvant synthesis). This amounts to 1.35×10^7 compounds to be analyzed per year. The value of ZULF would invariably be justified if the return on a spectrum is roughly 10% of a routine hourly NMR facility rate for high-field NMR (around \$50 per hour in an academic setting). This suggests roughly \$65 M in annual value for the pharmaceutical industry.

II. APPLICATION PARAMETERS

A. Molecular Specification

The scale and classical hardness of an NMR simulation are defined by a molecule’s nuclear spin Hamiltonian. These molecules are invariably tied to a given application, which may encompass molecules of varying complexity throughout its workflow. We will consider two classes of problems when formulating our estimates. Our first is a drug discovery workflow, which addresses a range of compounds from lead discovery through candidate synthesis. The second is a molecular fingerprinting application, where computationally generated ZULF spectra would be required for a set of molecules.

1. Drug Discovery Workflow

Molecular screening is a common strategy in drug discovery [48]. This approach evaluates a library of compounds for activity at one more biological targets in a semi-automated assay. These targets range in size from macromolecules like receptor proteins, ion channels, and enzymes to whole-cell or tissue preparations. This library may draw from molecu-

lar fragments, previously identified drug candidates, or large complex molecules. The smallest of these are fragments, which resemble the synthetic building blocks that comprise an actual drug [49]. Previous drug candidates or drug-like molecules are larger, and will be analogous in scale or complexity to actual pharmaceuticals. The largest screening candidates are often ‘natural products’, which are complex secondary metabolites from a range of organisms (fungi, bacteria, marine life, etc.) [50, 51]. While this chemical complexity may increase the utility of a natural product dataset, these molecules must often be deconstructed to identify key molecular features. The elucidation of natural product structures is often laborious and time consuming, making them a prime target for new spectroscopic methodology.

A workflow generally proceeds by screening these compounds until one or more ‘hits’ are identified [49?]. If these hits are fragments, they may be used as a starting point to design more substantial molecules that serve as drug candidates. Conversely, smaller segments of a natural product may be synthesized to find a minimal component for activity, termed a pharmacophore. Irrespective of the approach, the identification of this minimal component is a major goal. The structure–affinity or structure–activity relationship defined by extensions of this pharmacophore and biological activity is also of immense importance. Optimization of subject to these constraints will deliver a drug candidate or ‘lead’ compound.

A benchtop ZULF spectrometer could be useful for analyzing any of these molecular datasets. This would include rapidly assessing the structure of synthetic fragments and drug candidates, as well as complimenting high–field NMR studies of natural products. Thus, we assess overhead for common molecular fragments and screening libraries (the Maybridge RO3 Diversity and Screening collections), the top 300 small–molecule pharmaceuticals in the United States, and a curated collection natural products.

The complexity of nuclear spin Hamiltonians from this workflow is captured in Fig. 2.

2. Field Spectroscopy Workflow

Compact NMR spectrometers can be of high utility outside the laboratory. Plausible field settings are diverse, spanning from industrial manufacturing floors and clinical healthcare settings to forensic deployments and the austere environments of combat zones. We will consider this ZULF use case for a

range of applications. On one hand, we focus on explosives and nerve agents, where heteronuclear nitrogen and phosphorous NMR could be useful for identifying materials (particularly for novel, previously undetected substances). We also consider a forensic dataset containing drugs of abuse, which may be of interest to law enforcement and border protection. Finally, we generate estimates for molecular electronic materials with industrial relevance, with an emphasis on OLED and light–harvesting compounds. These represent a use case for industrial quality assurance and control. While we do not consider them as a separate dataset, many pollutants are comparable in size to our drug screening fragments.

B. Hamiltonian Parameters

Our molecular dataset includes Hamiltonians with both homonuclear, e.g., ^1H – ^1H , and heteronuclear, e.g., ^1H – ^{15}N , couplings. We will write J_{AB}^k to denote J –couplings by between nuclei of species A and B, where k is the number of bonds separating the coupled spins. For simplicity, we drop the isotopic label when it can be inferred from context (all nuclei are assumed to be the most abundant spin-1/2 isotope). To give a concrete example, the two–bond heteronuclear coupling between a proton ^1H and a carbon ^{13}C would be written as J_{CH}^2 . The same convention extends to dipolar couplings, which will be denoted by J_{AB}^D . Distances these are noted parenthetically or in the text when the context is clear. Finally, we use $\omega_i = 2\pi f_i$ to denote chemical shifts. Note that our Hamiltonian is written in terms of angular frequency, though chemical shifts and couplings will be specified in Hz or MHz. The will be understood by convention, allowing us to omit factors of 2π from expressions.

While a comprehensive treatment would utilize molecule–specific couplings based on experimental data, this is prohibitive the datasets that we consider. Instead, we use common reference values from the literature. These will match the established values in magnitude and thus be sufficient for resource analysis. Scalar J –couplings are taken from established sources [52], including the database used in the Spinach package [32]. Note that electronic structure methods can be used to estimate couplings when suitable tabulated data are unavailable [53, 54].

Our Hamiltonians address a robust spectroscopic limit, which means that we include a broad range of couplings to capture all parameters of relevance

to high-resolution spectroscopy. Unless otherwise noted (e.g., for the explosives dataset), we only consider the homonuclear coupling between protons ($J_{\text{HH}}^1, J_{\text{HH}}^2, J_{\text{HH}}^3$) and scalar heteronuclear couplings that may perturb the proton spin network ($J_{\text{CH}}^1, J_{\text{NH}}^1$). We also include heteronuclear dipolar couplings ($J_{\text{CH}}^D, J_{\text{NH}}^D$) since these can be detected in certain ZULF experiments. The low natural abundances of spin-active ^{13}C and ^{15}N isotopes make the detection of their large-scale spin networks unlikely without concerted effort. Nonetheless, we still include couplings among carbon and nitrogen nuclei ($J_{\text{CC}}^1, J_{\text{CN}}^1, J_{\text{CC}}^2$). This corresponds to isotopic enrichment of the sample or a limiting complexity for interpreting long, heavily sampled experiments. While this means that our datasets will overestimate the required overhead, the degree to which they do so not extreme (see Supplementary Material).

C. Spectroscopic Specifications

The proposed quantum simulations are intended to reproduce experimental ZULF NMR spectra. This section addresses how practical, experimental considerations would influence the choice of computational parameters.

1. Precision Thresholds

Our objective is to reconstruct $\langle S_{\text{tot}}^z(t) S_{\text{tot}}^z \rangle$ up to some maximal signal acquisition time t_{acq} while maintaining a finite spectral resolution $\Delta\omega$. This resolution is defined by the experimental spin-spin relaxation time $\Delta\omega \propto 1/T_2$, which can be used to set precision targets for quantum dynamics. Moreover, NMR experiments are subject to relaxation processes which translate to lower precision demands as t approaches T_2 . That is, if our spectral targets correspond to a dephasing rate of $\gamma = 1/T_2$, each spin will independently decohere with fidelity $F \sim \exp[-\gamma t]$. An ensemble of N spins will also incur a multiplicative error of F for each spin. Consequently, we need only reproduce our overall unitary evolution with an error threshold $(1 - \exp[-t/T_2]) \leq \epsilon(t) \leq (1 - \exp[-Nt/T_2])$. This will reduce the overhead for a qubitized time evolution, though constraints from amplitude amplification still require a minimum fidelity. Thus, we will impose a maximum error and thus minimum fidelity for the target time evolution unitary.

2. Relaxation and Timescale Parameters

A standing convention is to collect FID data up to an acquisition time of at least $t_{\text{acq}} = 3T_2$ for the slowest relaxing spin species. At this point 95% of the transverse magnetization profile will have been lost. While shorter sampling intervals can give the correct resonance peaks, they will be accompanied by satellite “ringing” artifacts. More typically, experiments will use times on the order of $t_{\text{acq}} = 5T_2$ for publication quality spectra, largely to capitalize on signal-to-noise concerns.

It is tempting to scour the literature for actual acquisition times. However, it is important to note that a practical choice is guided by other parameters, $t_{\text{acq}} = n_{\text{points}}/2W$, such as the desired spectral width W and the number of points n_{points} sampled in the signal. The experimental budget is also guided by a tradeoff between satisfying Nyquist sampling requirements and practical spectrometer availability. Thus, it is difficult to map literature parameters back to quantum simulations.

However, our objective is not to produce spectra that rival experimental data. Instead we seek to identify and correctly assign spectral resonances in classically intractable systems. Our proposed quantum methods are also free from relaxation effects, so there are no signal-to-noise issues. This means that the choice of simulation timescale is strictly guided by the need to capture experimentally relevant dynamical processes. Based on this, we will assume that most detectable coherence pathways will have developed by $t_{\text{max}} = T_2$, with those beyond that falling at or below the spectrometer detection threshold. However, we also provide precision datasets with a higher threshold of $t_{\text{max}} = 3T_2$ to accommodate more complex scenarios.

True ZULF experiments have T_2 values that can exceed those of conventional NMR by an order of magnitude or more. However, the higher $|\mathbf{B}_0|$ regime of low-field experiments correspond to shorter T_2 values, as will larger molecules. We adopt a representative T_2 value of 1 s for our spectra, which is a good compromise between these concerns. This also fixes our maximum simulation time. Note that we only leverage relaxation-induced fidelity constraints up to a maximum error of $\epsilon = 5.0 \times 10^{-3}$, which is necessary to ensure performance guarantees for robust oblivious amplitude amplification. However, it will only incur a logarithmic increase in overhead.

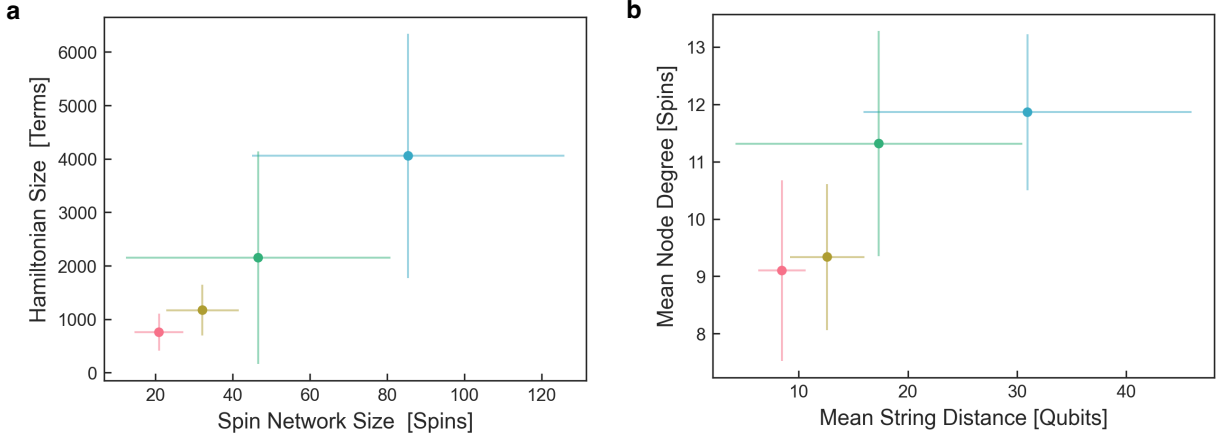


FIG. 2. **Characterization of the Nuclear Spin Hamiltonians.** (a) Nuclear Hamiltonian families according to the mean number of spins (data qubits) and Hamiltonian terms (Pauli strings); (b) Complexity of nuclear Hamiltonians, quantified by the mean distance between coupled qubits (e.g., between non-identity terms in a Pauli string) and the mean degree of each spin in the coupling network (e.g., the number of Hamiltonian terms containing the associated qubit). Bars represent standard deviations within the datasets. Colors correspond to molecular fragments (red), screening and synthetic intermediates (brown), marketed pharmaceuticals (yellow), and natural product leads (blue).

III. QUANTUM ALGORITHMS

Quantum signal processing (QSP) and its descendants are among the most efficient algorithms for fault-tolerant quantum simulation [55–58]. These qubitized methods can evolve a state up to time t with a precision of ϵ using $O(t + \log(1/\epsilon))$ queries to an oracle that block encodes a time-independent Hamiltonian. Spatial overhead is also efficient, as the block encoding can represent the Hamiltonian using $O(\log N)$ ancilla. We briefly review these methods as required to frame our analysis.

A. Block Encoding Strategy

We implement quantum dynamics using the quantum signal processing in the guise of the quantum eigenvalue transform (QET). A prerequisite is the ability to handle our nonunitary Hamiltonian H in a quantum circuit. This is accomplished by block encoding H in a larger unitary operator U_H ,

$$U_H = \begin{pmatrix} H & * \\ * & * \end{pmatrix}. \quad (10)$$

To utilize this, we define a signal state $|G\rangle \equiv |0^m\rangle$ with the requirement that,

$$H = (\langle G| \otimes I_n) U_H (|G\rangle \otimes I_n), \quad (11)$$

which effectively “extracts” the block that contains our target operator. This embedding must be a contraction in order to maintain unitarity. Stated differently, the spectral norm of the Hamiltonian must satisfy $\|H\| \leq 1$. This is untrue for most Hamiltonians, so we must perform a rescaling $H \mapsto \alpha^{-1}H$. Note that we are only concerned with the block that encodes H , and thus the behavior of our operations on other blocks can be left undefined.

Our nuclear spin Hamiltonian corresponds to a long-range Heisenberg model with a complicated topology. We must map this onto a one-dimensional qubit register for use with a quantum computer. Each term in $H = \sum_{i=1}^M c_i \Lambda_i$ will then correspond to a Pauli string with two non-identity factors,

$$\Lambda_i = I^{\otimes p} \otimes P_k \otimes I^{\otimes q} \otimes P_l \otimes I^{\otimes (N-p-q-2)}. \quad (12)$$

Since each Pauli string is unitary, H is inherently a linear combination of unitary operators (LCU).

Our block encoding follows a conventional strategy. We begin by defining a select oracle,

$$U_{\text{sel}} = \sum_i |i\rangle\langle i| \otimes \Lambda_i, \quad (13)$$

which gives access to a unitary Λ_i in the LCU through an ancillary signal register $|G\rangle$. A unary encoding is used to flag each Λ_i , which means that $|G\rangle$ must contain $m = \lceil \log_2 M \rceil$ qubits. Similarly,

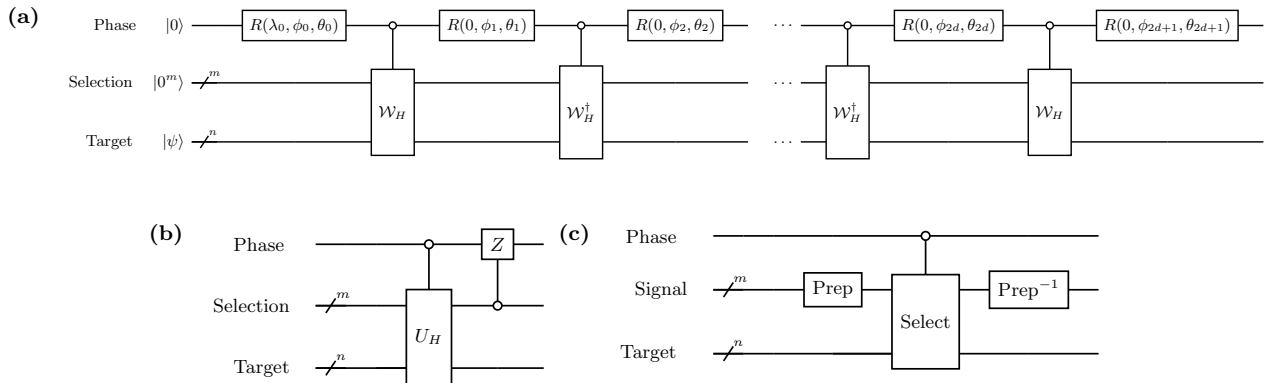


FIG. 3. **Circuits for a generalized quantum eigenvalue transform.** (a) A circuit implementation of the generalized quantum eigenvalue transform $\mathcal{O}_{\{\lambda, \phi, \theta\}}(H)$, for the case where we exponentiate $H \mapsto \exp[-\imath Ht]$ a block encoded Hamiltonian U_H via the walk operator \mathcal{W}_H . The signal processing rotations are $R(\lambda, \phi, \theta)$ operations in $SU(2)$, which we decompose according to a ZYZ convention. (b) Structure of the walk operator \mathcal{W} in terms of the block encoding U_H and multiccontrolled CZ gate. (c) Assembly of the block encoding U_H using Select and Prepare oracles.

we define a *prepare oracle*,

$$U_{\text{prep}} = \frac{1}{\sqrt{\|c\|_1}} \sum_i \sqrt{c_i} |i\rangle \langle 0^m| \quad (14)$$

which generates a weighted superposition via ancillary signal states. Here $\|c\|_1 = \sum_i |c_i|$ is the 1-norm of the coefficient set $\{c_i\}$. Note that we have singled out $|G\rangle = |0^m\rangle$ as a signal state for the prepare oracle. Our Hamiltonian is then delivered through a straightforward construction,

$$U_H = (U_{\text{prep}}^\dagger \otimes I_n) U_{\text{sel}} (U_{\text{prep}} \otimes I_n). \quad (15)$$

A circuit representation of this arrangement is depicted in Fig. 3b.

B. Quantum Eigenvalue Transform

Quantum signal processing (QSP) delivers a means to transform a single eigenvalue by a polynomial function $\lambda \mapsto f(\lambda)$ [55]. The quantum eigenvalue transform (QET) $\mathcal{O}_{\vec{\phi}}$ goes a step further and extends this over the spectrum of a normal operator [56–58]:

$$\mathcal{O}_{\vec{\phi}} : H \mapsto f(H) = \sum_{\lambda} f(\lambda) |\lambda\rangle \langle \lambda|. \quad (16)$$

This transformation is encoded using a series of phase angles $\{\phi_i\}$ that are classically optimized to

specify f . It is implemented using qubitized operators (see Appendix I) that include our block encoding U_H , a qubitized reflection operator $Z_{\Pi} = 2|G\rangle \langle G| \otimes I_n - I_m \otimes I_n$, and qubitized rotations $Z_{\Pi, \phi} = \exp[\imath \phi Z_{\Pi}]$. Putting these pieces together, the QET sequence is defined by the product,

$$\mathcal{O}_{\vec{\phi}} = e^{\imath \phi_0 Z_{\Pi}} \prod_{k=1}^d [U_H Z_{\Pi} e^{\imath \phi_k Z_{\Pi}}]. \quad (17)$$

In practice, the reflection can be incorporated into the encoding U_H or handled through a judicious choice of the phases.

While demonstrating robust asymptotic scaling, the use of $U(1)$ rotations leads to several fundamental restrictions. The most notable is that we can only encode strictly real or imaginary functions of definite parity. In the context of quantum dynamics, this means that we must implement the exponential evolution operator $x \mapsto \exp[\imath xt] = \cos(xt) + \imath \sin(xt)$ by combining individual circuits for the constituent sine and cosine transforms as an LCU.

Conventional QSP also places several restrictions on the encoded polynomials, which limits the ultimate transform to $H \mapsto \exp -\imath Ht/2$. Given an error ϵ in this encoding (via imprecision in the phase sequence), the probability of a useful outcome will be $p = \|\exp[\imath Ht]/2 \pm \epsilon\|^2$. This will lie close to 1/4 if ϵ is sufficiently small, potentially requiring repetition of the algorithm to get a workable result. A standard solution is to use robust oblivious amplitude amplification (ROAA), which can increase

the success probability to near unity [59, 60]. This technique promotes a QET circuit to a walk operator $W = \mathcal{O}_\phi(H)$, where the extended sequence $WRW^\dagger RW$ can suppress the failure probability to less than 2ϵ , where ϵ is our precision target. However, ROAA also triples the temporal overhead of the algorithm.

A recent alternative called generalized quantum signal processing (GQSP) [61] follows the spirit of early QSP proposals [55, 56, 62] while promoting the signal processing rotations to a series of SU(2) operations,

$$R(\lambda, \phi, \theta) = \begin{pmatrix} e^{i(\lambda+\phi)} \cos(\theta) & e^{i\phi} \sin(\theta) \\ e^{i\lambda} \sin(\theta) & -\cos(\theta) \end{pmatrix}. \quad (18)$$

Using these phases, it is possible to transform a block encoded operator H according to,

$$\left[\prod_{k=1}^d R(0, \phi_k, \theta_k) A \right] R(\lambda_0, \phi_0, \theta_0) = \begin{pmatrix} P(\mathcal{W}) & \cdot \\ Q(\mathcal{W}) & \cdot \end{pmatrix}, \quad (19)$$

where $A = |0\rangle\langle 0| \otimes \mathcal{W} + |1\rangle\langle 1| \otimes I$ is defined in terms of a walk operator $\mathcal{W} = Z_\Pi U_H$. This delivers a pair of complex polynomial transformations $|P(\mathcal{W})|^2 + |Q(\mathcal{W})|^2 = 1$ that are not subject to the same restrictions as conventional QSP methods. It also specifies an extremely simple and efficient algorithm to calculate both the required phase rotations and the form of one polynomial in terms of the other. These benefits compound for Hamiltonian simulation. This is because the spectral representation of $\mathcal{W} = \bigoplus_\lambda W_\lambda$ admits a particularly useful form,

$$W = \bigoplus_\lambda \begin{pmatrix} \lambda & \sqrt{1-\lambda^2} \\ -\sqrt{1-\lambda^2} & \lambda \end{pmatrix} \otimes |\lambda\rangle\langle\lambda|, \quad (20)$$

with eigenvalues $\exp[\pm i \cos^{-1} \lambda]$ in each qubitized eigenspace. While this holds true for any QSP method, the generalized scheme goes a step further by giving an efficient means to implement the transform $P(\mathcal{W}) = \exp[-iHt]$ so that,

$$P(W_\lambda) = \begin{pmatrix} e^{-it \cos(\cos^{-1}(\lambda))} & 0 \\ 0 & e^{-it \cos(-\cos^{-1}(\lambda))} \end{pmatrix}. \quad (21)$$

This is not possible with many conventional QSP schemes since since $P(x)$ is a complex polynomial of indefinite parity. An important consequence is that

separate QET transformations are no longer combined using an LCU, eliminating the need for amplification to boost the success probability. We adopt the generalized GQSP scheme for our time evolution circuits [63].

C. Phase Angle Generation

Our time evolution is implemented using phases that encode the polynomial $P(x)$ up to an error threshold ϵ . We can define a degree d Chebyshev polynomial approximation to trigonometric functions using the Jacobi–Anger expansion [55],

$$e^{it \cos(x)} \approx \sum_{n=-d}^d i^n J_n(t) e^{inx}, \quad (22)$$

and refine both the complimentary polynomial $Q(x)$ and SU(2) phase angles $(\lambda_k, \phi_k, \theta_k)$ using the algorithm of Ref. [61]. Here $J_n(t)$ is the n -th Bessel function of the first kind. This method can refine sequences up to 10^6 phases in roughly one minute using readily accessible classical hardware. This gives a series of $2d+1$ phase tuples for a degree d polynomial approximation, which is comparable to representing $x \mapsto \exp[ixt] = \cos(xt) + i \sin(xt)$ using standard methods (e.g., the symmetric phase sequence of [64]). The overall GQSP sequence will require $2d+1$ SU(2) rotations, $2d$ qubitized reflections, and $2d$ applications of our block encoding.

Taking the Jacobi–Anger expansion up to degree $d = e|\tau|/2 + \log_{10}(1/\epsilon)$ will give a truncation error bounded by ϵ . We use this fact in determining both optimization-based phases and the assignment of random phase values, which can be expeditious when constructing larger circuits. When optimizations are explicitly performed, we adopt convergence targets so that the overall phase sequence reproduces the target time–evolution unitary with fidelity $F = 1 - \epsilon$. While we generally use random angles for resource estimation, explicit determinations can be made using the pyLIQTR software suite [65, 66].

D. Circuit Implementation

We use a straightforward representation for GQSP which interleaves SU(2) rotations between controlled applications of the walk operator $\mathcal{W} = Z_\Pi U_H$. Note \mathcal{W} alternates with its adjoint between repetitions, which is required when encoding a polynomial expansion with terms of negative degree [61]. The walk

operator is defined by subsequent applications of a multicontrolled CZ operation and the block encoding U_H . This gives a multicontrolled $SU(2)$ rotation between repetitions of U_H or U_H^\dagger , similar to the qubitized rotation operator in a conventional QET sequence. The encoding U_H represents H as an LCU over Pauli strings using select and prepare oracles. We use a prepare oracle that combines QROM lookup with an alias sampling strategy [67], and which tolerates dirty ancilla outside of the selection register. This scheme approximates LCU coefficients to fixed bit precision at reduced T -complexity. Our select is more conventional, affording operators through unary iteration over a control register. Circuits are compiled to the Clifford+ T set before resource quantification, which permits operations with common quantum error correction layers schemes such as the surface code. All of these tasks are accomplished using the pyLIQTR software suite [65, 66] and its QUALTRAN extensions [68].

E. Observable Estimation and Sampling

In order to calculate ZULF spectra, we must have an initial spin population with a net magnetization along the z -axis. While a single product state like $|\psi(t=0)\rangle = \bigotimes_k |\uparrow\rangle_k$ might suffice for high-field simulations, the ZULF regime requires us to sample over an ensemble states with a net z -polarization (e.g., $|100\dots\rangle$, $|010\dots\rangle$, \dots). The most immediate way to accomplish this is by running a series of simulations that are initiated from each of these states. The resulting data can then be combined classically,

$$\mathcal{S}(t) = \sum_k \langle \psi_k(t) | S_{\text{tot}}^z | \psi_k(t) \rangle \quad (23)$$

$$= \sum_k \langle \psi_{0,k} | \mathcal{U}^{-1}(t) S_{\text{tot}}^z \mathcal{U}(t) | \psi_{0,k} \rangle \quad (24)$$

where $U(t) \exp[-iHt]$ is the unitary time evolution operator approximated by our QET circuit. Although the number of initial states will grow exponentially in N , the variance in this estimator is much smaller for our particular problem. More specifically, rudimentary statistical arguments can show that $\mathcal{S}(t)$ will be well-reproduced by sampling at most N^2 of these computational basis states. Reproducing this to a precision of ϵ_{meas} will require $O(1/\epsilon_{\text{meas}}^2)$ samples, so we can presume a worst-case scaling of $O(N^2/\epsilon_{\text{meas}}^2)$ for the number of required shots.

A more reasonable strategy is to prepare these states in superposition on our quantum computer,

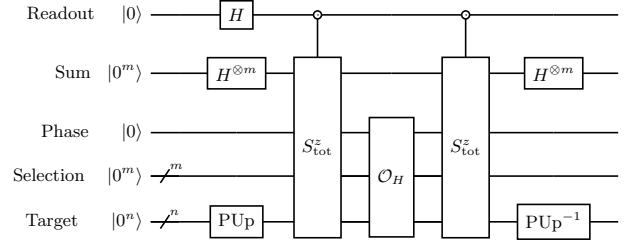


FIG. 4. **Correlation function estimator.** Circuit estimating the correlation function $\langle S_{\text{tot}}^z(t) S_{\text{tot}}^z \rangle$ based on phase kickback from total spin operators S_{tot}^z to the single-qubit Readout register. Time evolution is facilitated by the QET sequence \mathcal{O}_H while the PUP prepare oracle is used to prepare a superposition over spin-up states. The Hadamard transform $H^{\otimes m}$ does the same over all computational basis states, and serves as a prepare oracle for the unary encoding used by the total spin operator oracles.

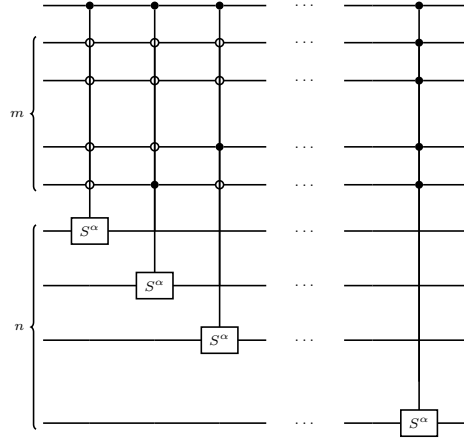


FIG. 5. **Total spin operator.** Circuit implementing the the total spin operator S_{tot}^α , where $\alpha \in \{x, y, z, +, -\}$ denotes the constituents. This arrangement requires $m = \lceil \log_2 n \rceil$ ancillary qubits, which can be shared with the signal register. The ancilla must be put into an equal superposition using a Hadamard transformation and uncomputed similarly after calculating the correlation function.

e.g., by generating a uniform superposition and filtering with inequality tests as in ???. The correlation function $\mathcal{S}(t) = \langle S_{\text{tot}}^z(t) S_{\text{tot}}^z \rangle$ can then be extracted using phase kickback from a pair of total spin operators followed by amplitude estimation. This strategy is depicted in Fig. 4 and Fig. 5. The simplest amplitude estimation strategy would use the Hadamard test with a $O(1/\epsilon_{\text{meas}}^2)$ overhead in the number of shots that estimate $\mathcal{S}(t)$. A robust error threshold

might be on the order of $\epsilon_{\text{meas}} = 0.01$ for a total of $N_{\text{shots}} = 10^4$ shots, while a more permissive value of $\epsilon_{\text{meas}} = 0.05$ gives a markedly reduced $N_{\text{shots}} = 400$ shots. Iterative phase or amplitude estimation procedures offer an alternative strategy, though these come with an additional repetition of the overall circuit [69].

Another sampling concern arises when considering the timepoints that are required to reconstruct $\mathcal{S}(t)$ and thus our target spectrum $\mathcal{S}(\omega)$. A naïve approach would uniformly sample $\langle S_{\text{tot}}^z(t) S_{\text{tot}}^z(0) \rangle$ with a timestep Δt so that $N_{\text{points}} = t_{\text{max}}/\Delta t$ is much greater than N . Based on experimental data, a typical, high-resolution spectrum might require 4096 points for reconstruction. However, the frequency domain spectrum $\mathcal{S}(\omega)$ is sparse, making it a prime candidate for compressed sensing methods [70]. These methods have proven effective for reducing overhead in NMR experiments [71–73]. This reduction can range from a factor of two for high-precision spectra [74] to a factor of 40 for crude spectra reconstructed in NISQ experiments [29]. Our goal is to reproduce the location of resonances and not mimic high-quality experimental data. Thus, a target of $N_{\text{points}} = 400$ seems suitable for most purposes, though as few as $N_{\text{points}} = 100$ could be permissible under many circumstances.

These data suggest that we must evaluate $N_{\text{shots}} \times N_{\text{points}}$ time evolution circuits to predict a spectrum. This corresponds to between 4×10^4 and 4×10^6 evaluations depending on the target application. However, many of these evolution circuits will have lower overhead than our explicit estimates, as the latter correspond to the maximal simulation time.

IV. RESOURCE ESTIMATES

Many resource estimation tasks focus on a small, curated set of problem inputs. This can make their conclusions susceptible to statistical biases that overestimate or underestimate the true algorithmic overhead. To obtain a more accurate measure, we have generated explicit time-evolution circuits for the nuclear spin Hamiltonians of 1×10^4 small molecules. While this is invariably skewed by our pool of application domains, it is nonetheless more representative than a hand-selected pool of representative molecules. When possible, we have selected established molecular datasets that are curated to ensure chemical diversity [75].

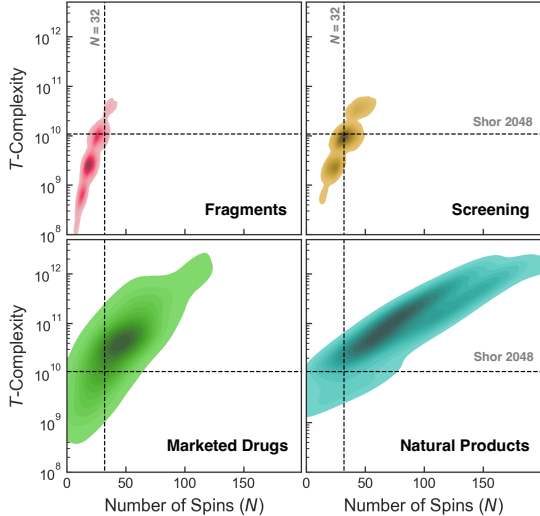


FIG. 6. **Temporal overhead vs. problem scale for drug discovery relevant spectra.** Estimated T -complexity versus number of spins for nuclear spin Hamiltonians that are relevant to drug-discovery. Contoured distributions are explicit counts for the longest QET circuit that is needed to reconstruct a 1D NMR spectrum sampled up to $t_{\text{max}} = T_2$. This corresponds to a single shot of the algorithm with robust oblivious amplitude amplification. Data reflect to small synthetic precursors and screening fragments ($N_{\text{mol}} = 3500$), larger screening fragments and synthetic intermediates ($N_{\text{mol}} = 5000$), top marketed pharmaceuticals ($N_{\text{mol}} = 253$), and challenging natural product leads ($N_{\text{mol}} = 44$). The horizontal dashed line is an estimated limit for Liouville space simulators ($N = 32$) and the vertical an estimated complexity for factoring 2048-bit integers using Shor’s algorithm [31]. Hamiltonians include a full complement of homonuclear and heteronuclear coupling terms, as described in the text. Note that the spin network size is smaller than the number of atoms in the molecule due to uncoupled or NMR-silent nuclei. A maximal error of $\epsilon = 5 \times 10^{-3}$ is budgeted when approximating the time evolution unitary with a QET sequence. A relaxation time of $T_2 = 1$ s is assumed for all molecules. The number of molecules in each dataset N_{mol} is noted parenthetically and contours are presented with 15 levels.

A. Drug Discovery Workflow

We begin by focusing on a drug-discovery workflow. The distribution of temporal overhead, which is quantified through the T -gate count, varies markedly between the difficult molecular datasets (Fig. 6). We can define a classically easy region based on a problem scale that will likely be limiting for Liouville-von Neumann simulators [32]

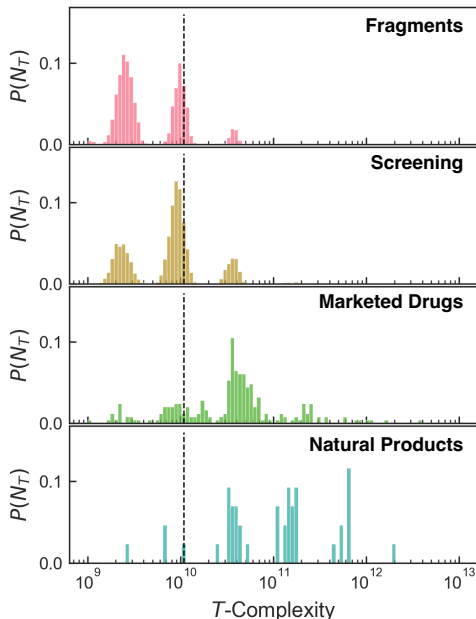


FIG. 7. **Temporal overhead distribution for drug discovery relevant spectra.** These data reflect the distribution $P(N_T)$ of T -gate counts N_T when using QET methods to simulate the associated nuclear quantum Hamiltonians. Instance parameters correspond to the data in Fig. 6, as do the number of molecules in each distribution. The vertical dashed line is the estimated fault-tolerant complexity for factoring 2048-bit integers using Shor’s algorithm [31].

when handling highly correlated spin Hamiltonians [25, 76]. An additional scale is given by the T -complexity for factoring 2048-bit integers using Shor’s algorithm, which has been a motivating application for quantum computation [31]. While all of our molecular classes happen to overlap with this region, roughly 79% of the small screening fragments and synthetic precursors fall within its confines (Fig. 8). Quantum simulations are less likely to be useful when predicting spectra for these compounds.

The outlook for high-throughput screening targets and more complex intermediates in drug synthesis is better. Here, roughly 44% of molecules might benefit from quantum computation in spectral prediction. This pool lies within an order of magnitude of the T -count for factoring 2048-bit integers (Fig. 7), suggesting that it could be a relatively near-term application for fault-tolerant quantum computation. This situation is even more optimistic for final drug candidates and natural product leads, where nearly 75% and 93% of compounds fall

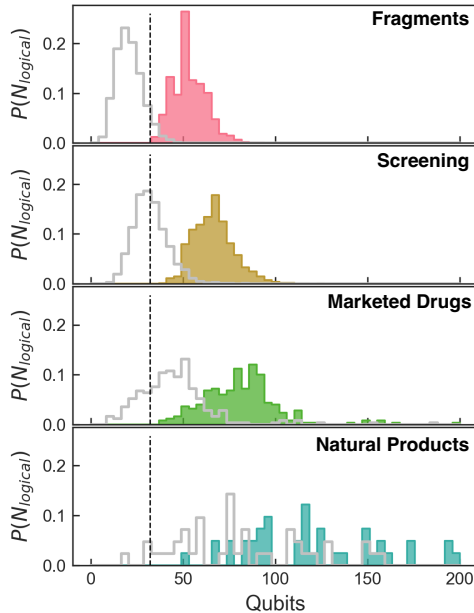


FIG. 8. **Spatial overhead distribution for drug discovery relevant spectra.** These data reflect the distribution P of logical (solid colors) and problem qubits (outline) that are required when using QET methods to simulate the associated nuclear quantum Hamiltonians. Instance parameters correspond to the data in Fig. 6

into the classically difficult regime, respectively. The total number of T -gates that are required for a single QET shot are also almost entirely within two orders of the 2048-bit factoring bound for both pools.

While natural products have broad magnetically-active spin systems, this is not directly reflected in the simulation complexity. Notably, the largest of these are almost twice the size of their largest pharmaceutical counterparts. This is reflected through both the number of problem qubits and the number of logical qubits that are used by the QET circuit (Fig. 8). Despite this, the average T -count for classically difficult natural product (9.07×10^{10} gates) and pharmaceutical (6.69×10^{10} gates) spin evolutions lie within a factor of two. We address the interplay between spin network complexity, entanglement structure, and simulability in a companion manuscript [77].

The modest logical qubit requirements and Shor-scale T -gate counts suggest that quantum computation might help enable the use of ZULF spectroscopy in drug discovery workflows on early fault-tolerant quantum computers. However, our algorithm must also be repeated in order to construct spectra. The use of compressed sensing techniques should enable

Molecule	Spins	Logical Qubits	T -Gates
Bacitracin	212	256	5.79×10^{11}
α -Conotoxin	197	241	5.11×10^{11}
Maitotoxin	420	437	1.77×10^{13}
Semaglutide	1921	1977	1.64×10^{14}
Ubiquitin	1112	1165	3.45×10^{13}

FIG. 9. **Single-shot dynamics estimates for biological macromolecules.** Estimated T -complexity and logical qubit count the single-shot generalized QET evolution of several biological macromolecules. Inputs are drawn from solved NMR ensembles in the Protein Data Bank (PDB IDs as follows, bacitracin: 4K7T, α -conotoxin: 2H8S, semaglutide: 4ZGM, ubiquitin: 1UBQ). Algorithm parameters are equivalent to those of Fig. 6

spectral prediction with roughly 400 timepoints, and our error threshold would require $O(1/\epsilon_{\text{meas}}^2)$ repetitions to obtain these to an estimation precision of ϵ_{meas} . If we assume $\epsilon_{\text{meas}} = 0.01$, which is likely on par with (or better than) the aggregate error in experimental data, this would naively necessitate 4×10^6 shots to predict a spectrum (or 4×10^7 shots under more relaxed constraints).

It is worth noting that only marginally greater overhead is found for very large natural products, peptide therapeutics and small proteins (Table. IV A). The latter have become feasible for ZULF with the advent of pulse sequences for total correlation spectroscopy (TOCSY) [78, 79]. These targeted methods can avoid the spectral crowding that would occur when taking ‘full-feature’ ZULF spectra of very large systems.

B. Molecular Fingerprinting Workflow

Our second workflow imagines how quantum computation could aid ZULF NMR spectrometers that are deployed in field applications. We consider a variety of use cases, including (i) explosive and CBRN detection (focusing on organophosphate nerve agents), (ii) the detection of illicit drugs, (iii) clinical screening applications in a healthcare setting, and (iv) quality control in the manufacture of organic electronics and optoelectronics. These results are summarized in Fig. 10. Here, we see more limited applicability for the explosive / CBRN and forensic datasets. However, some of these systems might benefit from higher-precision spectral calculations due to the unusual structures of the underlying molecules. This means that we cannot exclude the utility of quantum computation for these spectra.

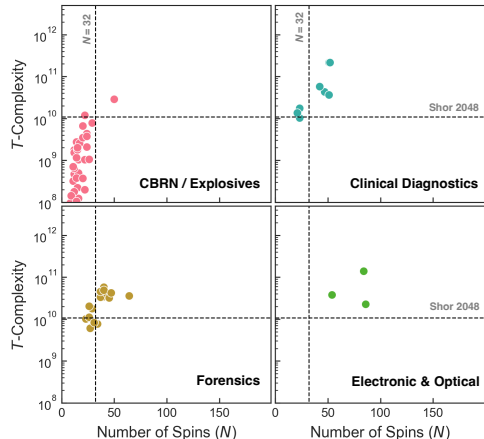


FIG. 10. **Resource overhead for molecular fingerprinting workflows.** Estimated T -complexity versus number of spins for problems involving ZULF field spectrometers.

Points correspond to the longest QET circuit that is needed to reconstruct a 1D NMR spectrum sampled up to $t_{\text{max}} = T_2$. This corresponds to a single shot of the algorithm with robust oblivious amplitude amplification. Data reflect explosive and CBRN detection (including organophosphorous nerve agents), (ii) the detection of illicit drugs, (iii) clinical screening applications in a healthcare setting, and (iv) quality control in the manufacture of organic electronics and optoelectronics. The horizontal dashed line is an estimated limit for Liouville space simulators ($N = 32$) and the vertical an estimated complexity for factoring 2048-bit integers using Shor’s algorithm [31]. Hamiltonians include a full complement of homonuclear and heteronuclear coupling terms, as described in the text. Nerve agents and explosives include additional homo- and heteronuclear couplings for nitrogen and phosphorous. A maximal error of $\epsilon = 5 \times 10^{-3}$ is budgeted when approximating the time evolution unitary. A relaxation time of $T_2 = 1$ s is assumed for all molecules. The number of molecules in each dataset N_{mol} is noted parenthetically and contours are presented with 15 levels.

Indeed, the fact that ZULF spectrometers could be used in a sequestered laboratory setting might make them advantageous when characterizing extremely hazardous or unstable materials. More optimistic prospects are seen for clinically relevant molecules and electronic materials.

V. CONCLUSIONS

We have demonstrated how quantum computation could augment the utility of certain low-field NMR spectroscopies. A unique aspect of this work

is that it addresses a large number of inputs and provides some of the only explicit, circuit based estimates (following [62]) for qubitized time evolutions using state-of-the-art algorithms. Based on our estimates, several classes of molecules remain at or beyond the limits of classical computation, with impacts that range from drug discovery to electronic materials.

Note that a quantum computer might have utility for classically tractable spectral prediction tasks, especially if it is sufficiently inexpensive and capable of high throughput. This is largely because many of these tasks do not benefit from the same classical high-performance computing workflows that impact frontier-scale quantum chemistry and condensed matter physics problems. These limitations are not just a consequence of resource availability or numerical methodology. Since spectral predictions will compliment individual experiments, a task that requires weeks of compute time would be diminished in utility for many small molecules (though utility would still hold for challenging targets like natural products and peptides). However, the hardness and scientific merit of these other HPC-amenable problems does not necessarily equate to direct economic impact.

Our effort follows several discussions of NMR simulation in a NISQ context [29]. Beyond low-field instruments, it has been proposed that quantum computation can find utility predicting macromolecular and solid-state materials spectra for high-field solid-state NMR. This is certainly plausible based on our observations, and is partially reflected through our peptide-based drug discovery instances. However, there are some challenges in addressing this regime, which originate in the disparate frequency scales between couplings and chemical shifts (which become relevant at high-field). This results in large Hamiltonian normalization factors and a linear increase in problem overhead, though this might be mitigated by certain mathematical transformations of the Hamiltonian. However, it also suggests a unique role for quantum computation in enabling ZULF spectrometers for this regime.

Another role for quantum simulation would lie in the design of pulse sequences for spectrometers [5]. This is inherently a quantum control problem, and the ability to tackle large spin systems could lead to unanticipated experimental techniques. However, both this and solid-state NMR require methods for the simulation of explicitly time-dependent Hamiltonians [80, 81].

While we have shown that a quantum computer could have utility in predicting low-field NMR spec-

tra, we do not make claims regarding quantum advantage. Notably, NMR experiments are characterized by relaxation, though this is substantially slower in low- and ultralow-field regimes. The inclusion of relaxation processes can reduce the required bond dimension – and thus classical overhead – for tensor network simulations [35, 36]. This can dequantize certain problems that are otherwise classically hard. While we cannot fully exclude this possibility here, it is significant that our Hamiltonians have less regularity and greater connectivity than many lattice models. This lends to greater operator entanglement and a commensurate increase in computational hardness. Moreover, these features can make several classical overhead-reduction strategies inapplicable. Our estimates also use relaxation parameters that are plausible yet on the faster end of the ZULF regime, though the general experimental distribution is poorly mapped at present. Based on these facts, it is unlikely that the more complicated spectra can be dequantized as readily as recent claims regarding quantum supremacy [82]. We consider these and related considerations in a separate manuscript [77].

As a final note, our estimates are generally pessimistic regarding the overhead that is required for spectral prediction. We include a broad range of homonuclear and heteronuclear coupling terms to approach the most taxing, high-precision scenarios. However, many experiments are performed for homonuclear proton networks, with the occasional inclusion of a few heteronuclear couplings with isotopic enrichment. This means that practical Hamiltonians would contain fewer terms, with a commensurate reduction in T -complexity.

VI. ACKNOWLEDGEMENTS

This material is based upon work supported by the Defense Advanced Research Projects Agency under Air Force Contract No. FA8702-15-D-0001. Any opinions, findings, conclusions or recommendations expressed in this material are those of the author(s) and do not necessarily reflect the views of the Defense Advanced Research Projects Agency.

VII. APPENDICES

1. Molecule Input Preparation

Small-molecule structures were prepared using molecular mechanics based calculations. Initial all-atom geometries were generated from a standard library of hybridization angles, as defined by the input connectivity. Geometries were then relaxed using conjugate gradient minimization in the classical

Merck molecular mechanics force field (MMFF94) [83]. No electrostatic or van der Waals cutoffs were applied, and optimizations were conducted to a relative energy gradient of 1×10^{-8} . This strategy is sufficient for most biomolecular simulations, where a finite environmental temperature will generally make electronic structure calculations unnecessary. These calculations were handled using the Open Babel toolkit [84]. Note that inputs based on solved protein NMR structures were used without geometry relaxation.

-
- [1] R. R. Ernst, G. Bodenhausen, and A. Wokaun, *Principles of Nuclear Magnetic Resonance in One and Two Dimensions* (Oxford University Press, 1990).
- [2] Y. Hu, K. Cheng, L. He, X. Zhang, B. Jiang, L. Jiang, C. Li, G. Wang, Y. Yang, and M. Liu, NMR-Based Methods for Protein Analysis, *Anal. Chem.* **93**, 1866 (2021).
- [3] M. Marušič, M. Toplishek, and J. Plavec, NMR of RNA — Structure and interactions, *Cur. Opin. Struc. Biol.* **79**, 102532 (2023).
- [4] C. Fontana and G. Widmalm, Primary Structure of Glycans by NMR Spectroscopy, *Chem. Rev.* **123**, 1040 (2023).
- [5] G. S. Rule and T. K. Hitchens, *Fundamentals of Protein NMR Spectroscopy* (Springer, 2006).
- [6] R. Sprangers, A. Velyvis, and L. E. Kay, Solution NMR of supramolecular complexes: providing new insights into function, *Nat. Methods* **4**, 697 (2007).
- [7] M. Weingarth and M. Baldus, Solid-State NMR-Based Approaches for Supramolecular Structure Elucidation, *Acc. Chem. Res.* **46**, 2037 (2013).
- [8] R. Rosenzweig and L. E. Kay, Solution NMR Spectroscopy Provides an Avenue for the Study of Functionally Dynamic Molecular Machines: The Example of Protein Disaggregation, *J. Am. Chem. Soc.* **138**, 1466 (2016).
- [9] R. Puthenveetil and O. Vinogradova, Solution NMR: A powerful tool for structural and functional studies of membrane proteins in reconstituted environments, *J. Biol. Chem.* **294**, 15914 (2019).
- [10] P. Bayer, A. Matena, and C. Beuck, NMR Spectroscopy of supramolecular chemistry on protein surfaces, *Beilstein J. Org. Chem.* **16**, 2505 (2020).
- [11] B. Reif, S. E. Ashbrook, L. Emsley, and M. Hong, Solid-state NMR spectroscopy, *Nat. Rev. Methods Primers* **1**, 2 (2021).
- [12] K. M. Cecil, Proton Magnetic Resonance Spectroscopy: Technique for the Neuroradiologist, *Neuroimag. Clin. N. Am.* **23**, 381 (2013).
- [13] G. Öz, *et al.*, Clinical Proton MR Spectroscopy in Central Nervous System Disorders, *Radiology*, 658.
- [14] J. M. Tognarelli, M. Dawood, M. I. F. Sharif, V. P. B. Grover, M. M. E. Crossey, I. J. Cox, S. D. Taylor–Robinson, and M. J. W. McPhail, Magnetic Resonance Spectroscopy: Principles and Techniques: Lessons for Clinicians, *J. Clin. Exp. Hepatol.* **5**, 320 (2015).
- [15] R. W. Brown, Y.-C. N. Cheng, E. M. Haacke, M. R. Thompson, and R. Venkatesan, *Magnetic Resonance Imaging: Physical Principles and Sequence Design* (Wiley, 2014).
- [16] J. M. Soares, R. M. aes, P. S. Moreira, A. Sousa, E. Ganz, A. Sampaio, V. Alves, P. Marques, and N. Sousa, A Hitchhiker’s Guide to Functional Magnetic Resonance Imaging, *Frot. Neurosci.* **10**, 515 (2016).
- [17] C. Westbrook and J. Talbot, *MRI in Practice* (Wiley, 2018).
- [18] J. Bernarding, G. Buntkowsky, S. Macholl, S. Hartwig, M. Burghoff, and L. Trahms, *J*-Coupling Nuclear Magnetic Resonance Spectroscopy of Liquids in nT Fields, *J. Am. Chem. Soc.* **128**, 714 (2006).
- [19] J. W. Blanchard, D. Budker, and A. Trabesinger, Lower than low: Perspectives on zero- to ultralow-field nuclear magnetic resonance, *J. Magn. Reson.* **323**, 106886 (2021).
- [20] S. J. DeVience, M. Greer, S. Mandal, and M. S. Rosen, Homonuclear *J*-Coupling Spectroscopy and Low Magnetic Fields using Spin-Lock Induced Crossing, *ChemPhysChem* **22**, 2128 (2021).
- [21] T. Theis, P. Ganssle, G. Kervern, S. Knappe, J. Kitching, M. P. Ledbetter, D. Budker, and A. Pines, Parahydrogen-enhanced zero-field nuclear magnetic resonance, *Nat. Phys.* **7**, 571 (2011).
- [22] J. W. Blanchard, M. P. Ledbetter, T. Theis, M. C. Butler, D. Budker, and A. Pines, High-Resolution Zero-Field NMR *J*-Spectroscopy of Aromatic Compounds, *J. Am. Chem. Soc.* **135**, 3607 (2013).
- [23] M. Emondts, M. P. Ledbetter, S. Pustelny, T. Theis, B. Patton, J. W. Blanchard, M. C. Butler, D. Budker, and A. Pines, Long-Lived Heteronuclear Spin-Singlet States in Liquids at a Zero Magnetic Field, *Phys. Rev. Lett.* **112**, 077601 (2014).

- [24] J. W. Blanchard, T. F. Sjolander, J. P. King, M. P. Ledbetter, E. H. Levine, V. S. Bajaj, D. Budker, and A. Pines, Measurement of untruncated nuclear spin interactions via zero- to ultralow-field nuclear magnetic resonance, *Phys. Rev. B* **92**, 220202(R) (2015).
- [25] S. Appelt, F. W. Häsing, U. Sieling, A. Gordji-Nejad, S. Glöggler, and B. Blümich, Paths from weak to strong coupling in NMR, *Phys. Rev. A* **81**, 023420 (2010).
- [26] The most straightforward digital quantum simulations will reproduce a pure state density matrix as opposed to the mixed state generated by relaxation operators. Instead, we treat relaxation through the decaying exponential factor in Eq. 2. Thus, the longitudinal and transverse magnetization profiles become equivalent for determining resonances in the NMR spectrum. It may be prudent to work with S^+ or S^- when developing pulse sequences due to the difference in objectives and potential methodology.
- [27] A. Karabanov, I. Kuprov, G. T. P. Charnock, A. van der Drift, L. J. Edwards, and W. Köckenberger, On the accuracy of the state space restriction approximation for spin dynamics simulations, *J. Chem. Phys.* **135**, 084106 (2011).
- [28] M. G. Algaba, M. Ponce-Martinez, C. Munuera-Javaloy, V. Pina-Canelles, M. J. Thapa, B. G. Take-tani, M. Leib, I. de Vega, J. Casanova, and H. Heimonen, Co-Design quantum simulation of nanoscale NMR, *Phys. Rev. Res.* **4**, 043089 (2022).
- [29] K. Seetharam, D. Biswas, C. Noel, A. Risinger, D. Zhu, O. Katz, S. Chattopadhyay, M. Cetina, C. Monroe, E. Demler, and D. Sels, Digital quantum simulation of NMR experiments, *Sci. Adv.* **9**, 1 (2023).
- [30] A. Burov, O. Nagl, and C. Javerzac-Galy, Towards quantum utility for NMR quantum simulation on a NISQ computer, arXiv:2404.17548 (2024).
- [31] C. Gidney and M. Ekerå, How to factor 2048 bit RSA integers in 8 hours using 20 million noisy qubits, *Quantum* **5**, 433 (2021).
- [32] H. J. Hogben, M. Krzystyniak, G. T. P. Charnock, P. J. Hore, and I. Kuprov, *Spinach* — A software library for simulation of spin dynamics in large systems, *J. Magn. Reson.* **208**, 179 (2011).
- [33] D. V. Savostyanov, S. V. Dolgov, J. M. Werner, and I. Kuprov, Exact NMR simulation of protein-size spin systems using tensor train formalism, *Phys. Rev. B* **90**, 085139 (2014).
- [34] M. C. Tayler and L. F. Gladden, Scalar relaxation of NMR transitions at ultralow magnetic field, *J. Magn. Reson.* **298**, 101 (2019).
- [35] Y. Zhou, E. M. Stoudenmire, and X. Waintal, What Limits the Simulation of Quantum Computers?, *Phys. Rev. X* **10**, 041038 (2020).
- [36] T. Ayrál, T. Louvet, Y. Zhou, C. Lambert, E. M. Stoudenmire, and X. Waintal, Density-Matrix Renormalization Group Algorithm for Simulating Quantum Circuits with a Finite Fidelity, *PRX Quantum* **4**, 020304 (2023).
- [37] A. Wilzewski, S. Afach, J. W. Blanchard, and D. Budker, A method for measurement of spin-spin couplings with sub-mHz precision using zero- to ultralow-field nuclear magnetic resonance, *J. Magn. Reson.* **284**, 66 (2017).
- [38] J. P. King, T. F. Sjolander, and J. W. Blanchard, Antisymmetric Couplings Enable Direct Observation of Chirality in Nuclear Magnetic Resonance Spectroscopy, *J. Phys. Chem. Lett.* **8**, 710 (2017).
- [39] D. A. Barskiy, M. C. D. Tayler, I. Marco-Ruis, J. Kurhanewicz, D. B. Vigneron, S. Cikrikci, A. Aydogdu, M. Reh, A. N. Pravdivtsev, J.-B. Hövener, J. W. Blanchard, T. Wu, D. Budker, and A. Pines, Zero-field nuclear magnetic resonance of chemically exchanging systems, *Nat. Commun.* **10**, 3002 (2019).
- [40] J. Ellis, R. Picazo-Frutos, O. Bondar, E. Cavallari, C. Carera, S. J. Barker, M. Utz, A. Herrero-Gomez, I. Marco-Ruis, M. C. D. Taylor, S. Aime, F. Reineri, D. Budker, and J. W. Blanchard, Enzymatic Reactions Observed with Zero- and Low-Field Nuclear Magnetic Resonance, *Anal. Chem.* **95**, 17997 (2023).
- [41] M. C. Tayler, J. Ward-Williams, and L. F. Gladden, NMR relaxation in porous materials at zero and ultralow magnetic fields, *J. Magn. Reson.* **279**, 1 (2018).
- [42] M. C. D. Taylor, J. Ward-Williams, and L. F. Gladden, Ultralow-field nuclear magnetic resonance of liquids confined in ferromagnetic and paramagnetic materials, *Appl. Phys. Lett.* **115**, 072409 (2019).
- [43] M. Jiang, T. Wu, J. W. Blanchard, G. Feng, X. Peng, and D. Budker, Experimental benchmarking of quantum control in zero-field nuclear magnetic resonance, *Sci. Adv.* **4**, aar6327 (2018).
- [44] M. Abobeih, J. Randall, C. Bradley, H. Bartling, M. Bakker, M. Degen, M. Markham, D. Twitchen, and T. Taminiau, Atomic-scale imaging of a 27-nuclear-spin cluster using a quantum sensor, *Nature* **576** (2019).
- [45] *Research and Development in the Pharmaceutical Industry*, Tech. Rep. (Congressional Budget Office, 2021).
- [46] (2023).
- [47] M. Christel, 2023 Pharm Exec Top 50 Companies, *Pharmaceutical Executive* **43**, 16 (2023).
- [48] J. P. Hughes, S. Rees, S. B. Kalindjian, and K. L. Philpott, Principles of early drug discovery, *Br. J. Pharmacol.* **162**, 1239 (2011).
- [49] D. A. Erlanson, S. W. Fesik, R. E. Hubbard, W. Jhanke, and H. Jhoti, Twenty years on: the impact of fragments on drug discovery, *Nat. Rev. Drug Discov.* **15**, 605 (2016).
- [50] D. J. Newman and G. M. Cragg, Natural Products as Sources of New Drugs over the Nearly four Decades from 01/1981 to 09/2019, *J. Nat. Prod.* **83**, 770 (2020).
- [51] A. G. Atanasov, S. B. Zotchev, V. M. Dirsch, the International Natural Product Sciences Taskforce,

- and C. T. Supuran, Natural products in drug discovery: advances and opportunities, *Nat. Rev. Drug Discov.* **20**, 200 (2021).
- [52] W. Kemp, *NMR in Chemistry: A Multinuclear Introduction* (Macmillan Education Limited, 1986).
- [53] D. Cremer and J. Gräfenstein, Calculation and analysis of NMR spin–spin coupling constants, *Phys. Chem. Chem. Phys.* **9**, 2791 (2007).
- [54] T. Helgaker, M. Jaszunski, and P. Swider, Calculation of NMR Spin–Spin Coupling Constants in Strychnine, *J. Org. Chem.* **81**, 11496 (2016).
- [55] G. H. Low and I. L. Chuang, Optimal Hamiltonian Simulation by Quantum Signal Processing, *Phys. Rev. Lett.* **118**, 010501 (2017).
- [56] G. H. Low and I. L. Chuang, Hamiltonian Simulation by Qubitization, *Quantum* **3**, 163 (2019).
- [57] A. Gilyén, Y. Su, G. H. Low, and N. Wiebe, Quantum singular value transformation and beyond: exponential improvements for quantum matrix arithmetics, in *Proceedings of the 51st Annual ACM SIGACT Symposium on Theory of Computing (STOC 2019)* (2019) pp. 193–204.
- [58] J. M. Martyn, Z. M. Rossi, A. K. Tan, and I. L. Chuang, Grand Unification of Quantum Algorithms, *PRX Quantum* **2**, 040203 (2021).
- [59] D. W. Berry, A. M. Childs, R. Cleve, R. Kothari, and R. D. Somma, Simulating Hamiltonian Dynamics with a Truncated Taylor Series, *Phys. Rev. Lett.* **114**, 090502 (2015).
- [60] J. M. Martyn, Y. Liu, Z. E. Chin, and I. L. Chuang, Efficient fully-coherent quantum signal processing algorithms for real-time dynamics simulation, *J. Chem. Phys.* **158**, 024106 (2023).
- [61] D. Motlagh and N. Wiebe, Generalized Quantum Signal Processing, arXiv:2309.01501.
- [62] R. Rines, K. Obenland, and I. Chuang, Empirical determination of the simulation capacity of a near-term quantum computer, arXiv:1905.10724 (2019).
- [63] Our practical use of the GQSP formalism actually corresponds to a quantum eigenvalue transform. However, we retain the name GQSP to maintain consistency with literature. However, it is currently unclear if GQSP can be extended to the more general context of the quantum singular value transform (QSVT).
- [64] Y. Dong, X. Meng, K. B. Whaley, and L. Lin, Efficient phase-factor evaluation in quantum signal processing, *Phys. Rev. A* **103**, 042419 (2021).
- [65] M. L. L. Quantum Algorithms Team, pyLIQTR: A Python library for fault-tolerant quantum algorithms.
- [66] Quantum Algorithms Team, MIT Lincoln Laboratory, pyLIQTR: A Python library for fault-tolerant quantum algorithms, arXiv:1234.56789 (2024).
- [67] R. Babbush, C. Gidney, D. W. Berry, N. Wiebe, J. McClean, A. Paler, A. Fowler, and H. Neven, Encoding Electronic Spectra in Quantum Circuits with Linear- T Complexity, *Phys. Rev. X* **8**, 041015 (2018).
- [68] G. Q. AI, QUALTRAN: A quantum algorithms translator. (2024).
- [69] D. Grinko, J. Gacon, C. Zoufal, and S. Woerner, Iterative quantum amplitude estimation, *Npj Quantum Inf.* **7**, 52 (2021).
- [70] D. Donoho, Compressed sensing, *IEEE Trans. Inf. Theory* **52**, 1289 (2006).
- [71] M. J. Bostock, D. J. Holland, and D. Nietlispach, Improving resolution in multidimensional NMR using random quadrature detection with compressed sensing reconstruction, *J. Biomol. NMR* **68**, 67 (2017).
- [72] M. Bostock and D. Nietlispach, Compressed sensing: Reconstruction of non-uniformly sampled multidimensional NMR data, *Concepts Magn. Reson. A* **46A**, e21438 (2018).
- [73] S. Robson, H. Arthanari, S. G. Hyberts, and G. Wagner, Nonuniform Sampling for NMR Spectroscopy, *Methods Enzymol.* **614**, 263 (2019).
- [74] F. Delaglio, G. S. Walker, K. A. Farley, R. Sharma, J. C. Hoch, L. W. Arbogast, R. G. Brinson, and J. P. Marino, Non-Uniform Sampling for All: More NMR Spectral Quality, Less Measurement Time, *Am. Pharm. Rev.* **20**, 339681 (2017).
- [75] R. A. E. Carr, M. Congreve, C. W. Murray, and D. C. Rees, Fragment-based lead discovery: leads by design, *Drug. Discov. Today* **10**, 987 (2005).
- [76] N. C. Menicucci and C. M. Caves, Local realistic model for the dynamics of bulk-ensemble NMR information processing, *Phys. Rev. Lett.* **2002**, 167901 (88).
- [77] J. E. Elenewki and A. Kalev, Forthcoming, (2024).
- [78] I. V. Khukov, A. S. Kiryutin, F. Ferrage, G. Buntkowsky, A. V. Yurkovskaya, and K. L. Ivanov, Total Correlation Spectroscopy across All NMR-Active Nuclei by Mixing at Zero Field, *J. Chem. Phys. Lett.* **11**, 7291 (2020).
- [79] A. S. Kiryutin, I. V. Zhukov, F. Ferrage, G. Bodenhausen, A. V. Yurkovskaya, and K. L. Ivanov, Sequential assignment of NMR spectra of peptides at natural isotopic abundance with zero- and ultra-low-field total correlation spectroscopy, *Phys. Chem. Chem. Phys.* **23**, 9715 (2021).
- [80] Y.-H. Chen, A. Kalev, and I. Hen, Quantum Algorithm for Time-Dependent Hamiltonian Simulation by Permutation Expansion, *PRX Quantum* **2**, 030342 (2021).
- [81] D. An, D. Fang, and L. Lin, Time-dependent Hamiltonian Simulation of Highly Oscillatory Dynamics and Superconvergence for Schrödinger Equation, *Quantum* **6**, 690 (2022).
- [82] J. Tindall, M. Fishman, E. M. Stoudenmire, and D. Sels, Efficient Tensor Network Simulation of IBM’s Eagle Kicked Ising Experiment, *PRX Quantum* **5**, 010308 (2024).
- [83] T. A. Halgren, Merck molecular force field. I. Basis, form, scope, parameterization, and performance of MMFF94, *J. Comput. Chem.* **17**, 490 (1996).

- [84] N. M. O'Boyle, M. Banck, C. A. James, C. Morley, T. Vandermeersch, and G. R. Hutchinson, Open Babel: An open chemical toolbox, *J. Cheminform.* **3**, 33 (2011).